SMBH accretion properties of radio-selected AGN out to z ~ 4

Delvecchio, Ivan; Smolčić, Vernesa; Zamorani, G.; Rosario, D. J.; Bondi, M.; Marchesi, S.; Miyaji, T.; Novak, Mladen; Sargent, M. T.; Alexander, D. M.; ...

Source / Izvornik: **Monthly Notices of the Royal Astronomical Society, 2018, 481, 4971 - 4983**

Journal article, Published version
Rad u časopisu, Objavljena verzija rada (izdavačev PDF)

https://doi.org/10.1093/mnras/sty2600

Permanent link / Trajna poveznica: https://urn.nsk.hr/urn:nbn:hr:217:226895

Monthly Notices of the ROYAL ASTRONOMICAL SOCIETY

MNRAS **481,** 4971–4983 (2018) doi:10.1093/mnras/sty2600
Advance Access publication 2018 September 24

SMBH accretion properties of radio-selected AGN out to $z \sim 4$

I. Delvecchio [1]★ V. Smolčić,[1] G. Zamorani,[2] D. J. Rosario,[3] M. Bondi,[4] S. Marchesi,[5] T. Miyaji,[6] M. Novak,[7] M. T. Sargent,[8] D. M. Alexander[3] and J. Delhaize[1]

[1]*Department of Physics, Faculty of Science, University of Zagreb, Bijenička cesta 32, 10002 Zagreb, Croatia*
[2]*INAF - Osservatorio di Astrofisica e Scienza dello Spazio - Bologna, Via Piero Gobetti 93/3, I-40129 Bologna, Italy*
[3]*Centre for Extragalactic Astronomy, Department of Physics, Durham University, South Road, Durham DH1 3LE, UK*
[4]*Istituto di Radioastronomia di Bologna – INAF, via P. Gobetti, 101, I-40129 Bologna, Italy*
[5]*Department of Physics and Astronomy, Clemson University, Clemson, SC 29634, USA*
[6]*IAUNAM-E (Instituto de Astronomía de la Universidad Nacional Aut ónoma de México Ensenada), Ensenada, Apdo. Postal 106, Ensenada BC 22800 Mexico*
[7]*Max-Planck-Institut für Astronomie, Königstuhl 17, D-69117 Heidelberg, Germany*
[8]*Astronomy Centre, Department of Physics and Astronomy, University of Sussex, Brighton BN1 9QH, UK*

Accepted 2018 September 14. Received 2018 August 21; in original form 2018 June 28

ABSTRACT

Exploring how radio-emitting active galactic nuclei (AGNs) behave and evolve with time is critical for understanding how AGN feedback impacts galaxy evolution. In this work, we investigate the relationship between 1.4 GHz radio continuum AGN luminosity ($L_{1.4}^{\rm AGN}$), specific black hole accretion rate (s-BHAR, defined as the accretion luminosity relative to the galaxy stellar mass), and redshift, for a luminosity-complete sample of radio-selected AGNs in the VLA COSMOS 3 GHz Large Project. The sample was originally selected from radio-continuum observations at 3 GHz, and includes about 1800 radio AGNs identified via ($>2\,\sigma$) radio-excess relative to the infrared-radio correlation of star-forming galaxies. We further select a subsample of over 1200 radio AGNs that is complete in $L_{1.4}^{\rm AGN}$ over different redshift ranges, out to $z \sim 4$, and use X-ray stacking to calculate the average s-BHAR in each $L_{1.4}^{\rm AGN}$–z bin. We find that the average s-BHAR is independent of $L_{1.4}^{\rm AGN}$, at all redshifts. However, we see a strong increase of s-BHAR with redshift, at fixed $L_{1.4}^{\rm AGN}$. This trend resembles the strong increase in the fraction of star-forming host galaxies [based on the $(NUV - r)/(r - J)$ colours] with redshift, at fixed $L_{1.4}^{\rm AGN}$. A possible explanation for this similarity might imply a link between average AGN radiative power and availability of cold gas supply within the host galaxy. This study corroborates the idea that radio-selected AGNs become more radiatively efficient towards earlier epochs, independently of their radio power.

Key words: galaxies: active – galaxies: jets – galaxies: nuclei – radio continuum: galaxies.

1 INTRODUCTION

Several studies have highlighted that active galactic nuclei (AGNs) are key ingredients to shape the properties and evolution of galaxies (see a comprehensive review by Hickox & Alexander 2018). In particular, it is widely accepted that every galaxy hosts a supermassive black hole (SMBH) at its centre, which may occasionally impact the surrounding interstellar medium, heating up the gas reservoirs within the galaxy, and possibly suppressing the formation of new stars (e.g. Sanders et al. 1988; Hopkins et al. 2008). During these episodes of AGN-driven feedback, enormous amounts of energy can be released in radiative and mechanical forms, which are commonly referred to as 'quasar mode' and 'jet mode', respectively (e.g. Heckman & Best 2014). On the one hand, the 'quasar mode' is commonly associated with radiatively efficient (>1 per cent Eddington) accretion, which is fuelled by cold gas inflows on to a standard, geometrically thin and optically thick accretion disc (Shakura & Sunyaev 1973), and over relatively short time-scales (<100 Myr). On the other hand, the 'jet-mode' phase is characterized by radiatively inefficient (≪1 per cent Eddington, also named 'advection-dominated accretion flow', ADAF; e.g. Narayan & Yi 1994), long lasting (∼Gyr time-scales) accretion episodes, likely fuelled via hot gas, that might generate powerful jets extending out to >kpc scales (e.g. Bower et al. 2006; Hardcastle, Evans & Croston 2007; Best & Heckman 2012).

Numerical simulations suggest that these two phases occur over different time-scales (Myr versus Gyr), spatial scales (pc versus >kpc), and possibly over distinct evolutionary stages of the AGN-galaxy lifecycle (e.g. Fanidakis et al. 2012). None the less, both

★ E-mail: ivan.delvecchio87@gmail.com

stages are postulated in semi-analytical models (e.g. Croton et al. 2016) in order to regulate the galaxy growth, and to reproduce the colours, stellar mass, and demography of today's massive galaxies (e.g. Benson et al. 2003; Hopkins et al. 2008).

Observational studies attempting to test the above scenario have collected large samples of AGNs across different wavelengths. While optical, mid-infrared (MIR), and X-ray-selected AGNs are sensitive to relatively high Eddington ratios ($\lambda_{\rm edd} \gtrsim 1$ per cent), radio observations can trace the non-thermal synchrotron emission powered by AGN-driven jets in the radiatively inefficient regime. Therefore, multiwavelength diagnostics are paramount to investigating the physical nature of each source.

In their comprehensive study, Hickox et al. (2009) selected AGNs separately at X-ray, radio, and MIR wavelengths in the Boötes field out to $z \sim 0.8$, and analysed their host-galaxy properties. They found that the relative overlap between X-ray, radio, and MIR-selected AGNs is typically small (<10 per cent). The fractional overlap depends on the relative depth of the matched samples, as well as on the reliability and completeness of each AGN selection criterion (e.g. Mendez et al. 2013). In addition, a small relative overlap may imply that different criteria are sensitive to intrinsically distinct SMBH and galaxy populations.

This was further investigated by Goulding et al. (2014) out to $z \sim 1.4$, who confirmed that radio-selected AGNs with 1.4 GHz luminosity $L_{1.4} > 10^{24.8}$ W Hz^{-1} are distinguishable from the other AGN classes concerning the properties of their hosts. Indeed, galaxies hosting radio AGNs were found to be systematically more massive and less star forming than those hosting X-ray and MIR AGNs. These and other studies (Mendez et al. 2013) support the idea that the physical mechanisms driving the triggering of an AGN might be linked to the properties of its host, especially the availability of cold gas supply, which is essential to fuel both star formation and radiatively efficient accretion on to the central SMBH (Aird, Coil & Georgakakis 2018). However, those panchromatic studies selected relatively bright radio AGNs via a conservative cut in $L_{1.4}$, thus potentially missing a large fraction of lower luminosity radio AGNs, which might display a different behaviour. In this respect, deep radio surveys allow us to explore the faint (sub-mJy) radio source population with unprecedented detail, providing valuable insights into the origin of radio emission.

In the Extended Chandra Deep Field South (E-CDFS), deep observations were carried out with the Very Large Array (VLA) at 1.4 GHz down to 37 μJy beam^{-1} (at 5σ; Miller et al. 2013). Exploiting these data, Bonzini et al. (2013, 2015) carried out a detailed analysis of the multiwavelength properties of radio sources in the sub-mJy regime. They found that below 200 μJy at 1.4 GHz, the radio source counts are dominated by normal (i.e. non-AGN) galaxies, whose radio emission originates from the diffusion of cosmic ray electrons produced in supernova remnants within young star-forming regions.

This aspect has been investigated further with the VLA-COSMOS 3 GHz Large Project (Smolčić et al. 2017a), in which unprecedently deep radio 3 GHz observations were carried out across the full COSMOS field (Scoville et al. 2007) down to ∼11.5 μJy beam^{-1} (5σ limit). This survey allowed us to put more stringent constraints on the composition of the faint radio source population, thus confirming a change in the dominant population at 1.4 GHz flux density of 200 μJy (e.g. Padovani et al. 2015). While star-forming galaxies dominate at fainter fluxes, radio-emitting AGNs take over at higher flux density levels (Smolčić et al. 2017b). These findings do not necessarily rule out the presence of widespread AGN emission below 200 μJy (see also Molnár et al. 2018), but mainly identify the dominant source of radio emission. Pushing this issue towards even fainter radio fluxes requires high-angular resolution radio observations, in order to pinpoint the circumnuclear radio AGN emission. This approach has already proved to be successful by exploiting recent data from the Very Long Baseline Interferometry (VLBI) in the COSMOS field (Herrera Ruiz et al. 2017), and will definitely become mainstream in the next decade with the Square Kilometer Array.

However, it is well established that the radio source population above 200 μJy consists of composite radio sources, whose 1.4 GHz emission arises from both star formation and SMBH accretion (Smolčić et al. 2017b). The fractional contribution due to AGN activity increases towards brighter radio fluxes, however at least two radio AGN populations have been identified at these flux densities (e.g. see review by Padovani 2016). Historically, radio AGNs have been classified as 'Radio Quiet' (RQ) or 'Radio Loud' (RL) AGNs, based on the dominant source of radio emission, namely star formation in RQ and AGN activity in RL sources, respectively. This classification has been widely used in the literature, often adopting alternative nomenclatures or selection criteria (Smolčić et al. 2009; Best & Heckman 2012; Padovani 2016; Mancuso et al. 2017), which eventually boils down to whether an excess in radio emission is significant relative to the one expected from star formation within the host. In such a case, 'radio-excess AGNs' (e.g. Del Moro et al. 2013; Delvecchio et al. 2017, D17 hereafter) display radio emission that is mainly driven by active jets, and may be used as indicators of the AGN kinetic power (e.g. Willott et al. 1999; Cavagnolo et al. 2010).

Nevertheless, radio-excess AGNs might display quite heterogeneous SMBH accretion properties. Several studies focusing on the radio emission of AGN-dominated sources pointed out that these objects can span a wide range of SMBH accretion rates (e.g. Padovani et al. 2015), gradually switching their dominant accretion mode between radiatively efficient and inefficient depending on $\lambda_{\rm edd}$. On the one hand, if $\lambda_{\rm edd} >$ few per cent, the radio jet power is driven by a radiatively efficient accretion disc, possibly shining in X-ray and MIR wavelengths, and with intense optical emission lines (e.g. Best & Heckman 2012). On the other hand, if $\lambda_{\rm edd} \ll$ few per cent, the gas fuelling on to the central SMBH is radiatively inefficient, therefore the AGN bolometric output comes predominantly in a kinetic form.

The connection between SMBH accretion and jet production in AGNs has been largely investigated in optically selected quasars (e.g. Kellermann et al. 1989; Cirasuolo et al. 2003; Baloković et al. 2012), taken from the Sloan Digital Sky Survey and cross-matched with FIRST data at 1.4 GHz. Although the existence of two physically distinct accretion modes in radio AGNs is still debated, a typical fraction as low as ∼10 per cent of optically selected quasars were detected by FIRST, suggesting a broad underlying radio power distribution.

However, no systematic analysis of the SMBH accretion rate of radio AGNs has been carried out at relatively faint radio fluxes (sub-mJy) and beyond the local Universe. Exploring these aspects down to fainter sources and towards higher redshift is crucial to answer the key question: 'Does the SMBH accretion rate of radio AGNs depend on radio power and cosmic time?' Addressing this issue requires a complete, statistical sample of radio-selected AGNs spanning a wide redshift and luminosity range, as provided by the VLA-COSMOS 3 GHz Large Project (Smolčić et al. 2017a).

In this paper, we explore the average SMBH accretion rate of radio-selected AGNs in the COSMOS field, by exploiting the latest

Chandra data as a function of both radio power and redshift. Our sample is one of the deepest and most complete data sets of radio-excess AGNs available to date.

The paper is structured as follows. In Section 2 we describe our sample selection and the identification of radio-excess AGNs. The full analysis of X-ray imaging and the average emission obtained from *Chandra* stacking are presented in Section 3. The derivation of SMBH accretion rate estimates, as well as their relationship with radio luminosity and redshift, is presented and discussed in Section 4. The interpretation of our results and the comparison with previous works in the literature are given in Section 5. Finally, we outline our concluding remarks in Section 6.

Throughout this paper, we assume a Chabrier (2003) initial mass function and a flat cosmology with $\Omega_{\rm m} = 0.30$, $\Omega_{\rm m} = 0.70$, and $\Omega_\Lambda = 70\,{\rm km\,s^{-1}\,Mpc^{-1}}$ (Spergel et al. 2003). Magnitudes are given in the AB system (Oke 1974).

2 SAMPLE SELECTION AND CLASSIFICATION

In this Section we describe our parent sample of VLA 3 GHz sources in the COSMOS field, their multiwavelength counterparts, and the approach used to identify radio AGNs. The final sample of radio-excess AGNs that will be studied in the rest of this paper is introduced in Section 2.3.

2.1 Multiwavelength photometry and redshifts

2.1.1 Optical-IR counterparts

The sample analysed in this work was originally selected using new, highly sensitive 3 GHz observations with the Karl G. Jansky Very Large Array (VLA) across 2.6 square deg of the COSMOS field, namely the 'VLA-COSMOS 3 GHz Large Project' (Smolčić et al. 2017a). This is currently the deepest extra-galactic radio survey ever conducted across a medium-area field like COSMOS. We detected 10 830 radio sources (at $\geq 5\,\sigma$) down to an average rms of about 2.3 μJy beam^{-1}, with a 0.75 arcsec resolution element.

The plethora of ancillary data available in the COSMOS field enabled us to cross-match the vast majority (about 90 per cent) of our 3 GHz selected sources with optical/NIR counterparts taken from the COSMOS2015 catalogue (Laigle et al. 2016), over an effective unmasked area of 1.77 deg^2, which yielded a total of 7729 matches. The counterpart association method is detailed in Smolčić et al. (2017b). Briefly, for each radio source we searched for all potential counterparts within a radius of 0.8 arcsec, and calculated the false-match probability of each pair by accounting for the optical/IR magnitude of each counterpart candidate. We selected the most likely counterpart via a neighbour matching algorithm, combined with a threshold in the false-match probability (<20 per cent), in order to minimize the fraction of spurious associations (∼1 per cent). We verified that over 90 per cent of matches are unique and found within 0.4 arcsec (i.e. half-beam size), thus ensuring a robust association.

2.1.2 X-ray counterparts

In addition to the optical to far-infrared (FIR) photometry taken from the COSMOS2015 catalogue, we used the most recent X-ray data to identify AGNs in our sample. X-ray sources were taken from the *Chandra* COSMOS-Legacy survey (Civano et al. 2016, Marchesi et al. 2016a). The X-ray catalogue was already cross-matched to the COSMOS2015 catalogue, as detailed in Laigle et al. (2016), yielding 906/7729 (around 12 per cent) sources in common with our radio-selected sample. For each X-ray source, count rates, fluxes, and absorption-corrected X-ray luminosities are available (Marchesi et al. 2016a) in the soft [0.5–2 keV], hard [2–10] keV, and full [0.5–10] keV bands.

2.1.3 Redshift measurements

A spectroscopic or a photometric redshift was assigned to each of the 7729 radio sources with a counterpart in the COSMOS2015 catalogue (see D17). Briefly, spectroscopic redshifts were taken from the COSMOS spectroscopy master catalogue (Mara Salvato, priv. comm.). If a spectroscopic redshift was not available or of poor quality, a photometric measurement was taken instead from the COSMOS2015 catalogue (Laigle et al. 2016), which was derived using the LE PHARE SED-fitting code (Arnouts et al. 1999; Ilbert et al. 2006) and employing galaxy templates from the library of Bruzual & Charlot (2003). Special care was taken for the computation of photometric redshifts of X-ray detected sources (Marchesi et al. 2016a), which were derived by adopting a hybrid library of AGNs and galaxy templates, which is more suitable for possible AGN-dominated sources (Salvato et al. 2009, 2011). For X-ray detected sources, we preferred this latter approach rather than relying on galaxy templates only.

Spectroscopic redshifts were collected for 2734/7729 sources (around 35 per cent), which we used to test the accuracy of the photometric redshifts. We found an excellent agreement, with a median absolute deviation $\langle|\Delta\, z/(1+z)|\rangle = 0.010$, which increases to 0.035 at $z > 3$ (see also Laigle et al. 2016). The full list of 7729 radio sources containing redshift and multiwavelength information is publicly retrievable on the IPAC/IRSA data base.[1]

2.2 Radio-excess AGN identification

In this Section we describe the procedure used to identify radio-excess AGNs in our sample.

The full sample of 7729 radio sources was analysed with the spectral energy distribution (SED) fitting tool SED3FIT (Berta et al. 2013), which decomposes the broad-band SED using galaxy templates from MAGPHYS (da Cunha, Charlot & Elbaz 2008), with the addition of AGN templates (Fritz, Franceschini & Hatziminaoglou 2006; Feltre et al. 2012). This approach allowed us to derive AGN-corrected galaxy parameters, such as infrared luminosity ($L_{\rm IR}$), star formation rate (SFR), and stellar mass ($M_\star$) for each radio source.

As radio emission may arise from processes related to both star formation and AGN activity, we used the infrared–radio correlation (IRRC) to statistically decompose the total radio emission, and isolate the AGN-related radio contribution. The IRRC is often expressed in terms of the parameter $q_{\rm SF}$, defined as the logarithmic ratio between the SF-related IR luminosity ($L_{\rm IR}^{\rm SF}$) and the total 1.4 GHz radio luminosity ($L_{1.4}$). In particular, we followed the latest IRRC derivation of Delhaize et al. (2017), who exploited the most recent radio data from the VLA-COSMOS 3 GHz Large Project (Smolčić et al. 2017a) and FIR data from the *Herschel Space Observatory* (Pilbratt et al. 2010). *Herschel* photometry was taken with the *Photoconductor Array Camera and Spectrometer* (PACS; 100 and 160 μm; Poglitsch et al. 2010) as part of the *PACS Evolutionary Probe* (Lutz et al. 2011), and with the *Spectral and Photometric Imaging Receiver* (250, 350, and 500 μm; Griffin et al. 2010) from

[1] http://irsa.ipac.caltech.edu/data/COSMOS/tables/vla/

the *Herschel Multi-tiered Extragalactic Survey* (Oliver et al. 2012). *Herschel* fluxes were extracted and de-blended via a PSF fitting algorithm using *Spitzer* 24 μm positional priors.

Each $L_{\rm IR}^{\rm SF}$ estimate was calculated from the optical to FIR SED-fitting decomposition (see D17), after disentangling the AGN-related emission from the host-galaxy light in the total IR (rest 8–1000 μm) regime. On the other hand, $L_{1.4}$ was calculated from the integrated 3 GHz flux and *K*-corrected to 1.4 GHz by assuming a power-law radio spectrum of the shape $S_\nu \propto \nu^\alpha$. The spectral slope α was taken from the observed 1.4 GHz flux (Schinnerer et al. 2010) if the source was detected at 1.4 GHz; otherwise, it was imposed to $\alpha = -0.7$ (e.g. Condon 1992; Murphy 2009), consistently with the average slope measured for our 3 GHz sources (Delhaize et al. 2017).

Given that the infrared emission was already corrected for a possible AGN contribution, the IRRC can be used as a benchmark to quantify the excess in radio emission as a tracer of radio AGN activity. In fact, the larger the offset from $q_{\rm SF}$, the larger the AGN contribution in radio. The above IRRC presented in Delhaize et al. (2017) was calibrated on a sample of star-forming galaxies, after disregarding X-ray and mid-infrared AGNs (see their Section 4.3), while still incorporating possible AGN-dominated sources in radio. While their inclusion does not impact the overall redshift trend of $q_{\rm SF}$ for star-forming galaxies (Delhaize et al. 2017), this might drag the overall $q_{\rm SF}$–z trend down, thus washing out a possible residual AGN contribution in the radio band, which might be instead relevant for our analysis. Therefore, we re-calculated the IRRC after removing the $>2\,\sigma$ outliers from either sides of the cumulative $q_{\rm SF}$ distribution, using a double-censored survival analysis to account for upper and lower limits.

This approach allowed us to partly purify the sample of star-forming galaxies from possible radio AGN contribution, leading to the following best-fitting trend: $q_{\rm SF} = (2.80 \pm 0.02) \cdot (1 + z)^{-0.12 \pm 0.01}$. This relation is slightly flatter than that originally presented in Delhaize et al. (2017), but largely consistent with independent derivations from the literature (e.g. Ivison et al. 2010; Sargent et al. 2010; Magnelli et al. 2015; Calistro Rivera et al. 2017).

This expression was then used to identify 'radio-excess AGNs': for consistency, a source was defined as a 'radio-excess AGN' (or REx AGN) if displaying *a* $>2\,\sigma$ offset from the above IRRC, where σ is the observed dispersion around best-fitting IRRC (∼0.35 dex, consistent with the dispersion found by Delhaize et al. 2017). This threshold ensures low contamination from star-forming galaxies (2.5 per cent), and it is highly sensitive to AGN-dominated (>80 per cent of the total 1.4 GHz emission) sources in the radio band. For each radio-excess AGN, the SF-related radio emission was quantified from the above $q_{\rm SF}(z)$ trend, and subtracted from the observed $L_{1.4}$, leaving us with the AGN-related radio luminosity at 1.4 GHz ($L_{1.4}^{\rm AGN}$). We note that our results would not change significantly if adopting the original Delhaize et al. (2017) relation instead; however, our purified $q_{\rm SF}(z)$ trend is more consistent with the adopted definition of a radio-excess AGN.

2.3 Final sample of radio-excess AGNs

The sample of radio-excess AGNs defined in the previous Section includes 1811 sources in total. Fig. 1 shows $L_{1.4}^{\rm AGN}$ of each source as a function of redshift. The black dashed line marks the $5\,\sigma$ luminosity limit of our survey at 3 GHz, converted to 1.4 GHz by assuming a spectral index $\alpha = -0.7$ (see Section 2.2). Black circles are shown for both X-ray detected (filled circles) and X-ray undetected (empty circles) radio-excess AGNs. The fraction of radio AGNs that are X-ray detected is only 16 per cent (286/1811) down to an average flux limit of $\sim 2 \times 10^{-15}$ erg s^{-1} cm^{-2} in the [0.5–8] keV band. Our sample of radio-excess AGNs is highly conservative (see Section 2.2), while spans five orders of magnitude in $L_{1.4}^{\rm AGN}$ over the redshift range $0 < z \lesssim 5$. This sample is notably deeper in 1.4 GHz luminosity than other works identifying AGN-dominated radio sources (e.g. Hickox et al. 2009; Padovani et al. 2015), which allows us to investigate SMBH accretion across a wide and well-defined radio source population at different cosmic epochs.

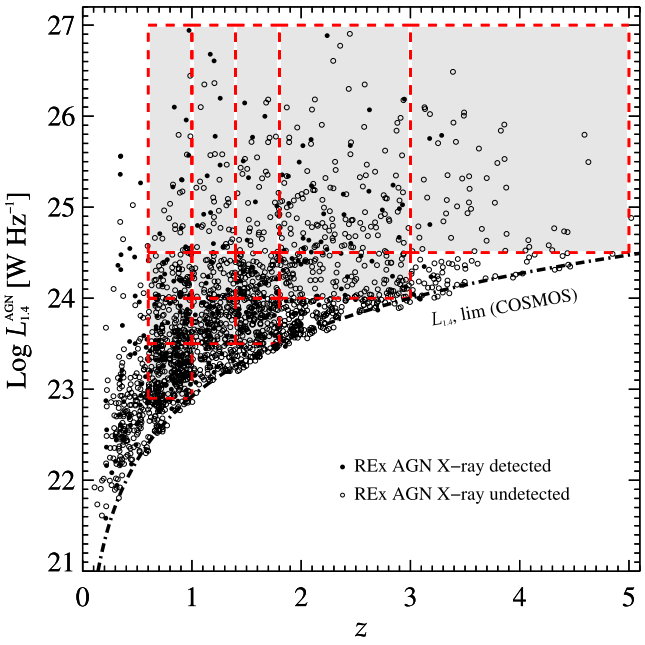

Figure 1. AGN-related 1.4 GHz radio luminosity ($L_{1.4}^{\rm AGN}$) as a function of redshift. The black dashed line marks the $5\,\sigma$ luminosity limit of the survey, scaled to 1.4 GHz by assuming a spectral index $\alpha = -0.7$. Black circles indicate radio-excess AGNs, both X-ray detected (filled circles) and undetected (empty circles). Shaded areas indicate the 13 complete $L_{1.4}^{\rm AGN}$–z bins analysed in this work.

We aim at investigating the average SMBH accretion properties of radio-excess AGNs by exploiting *Chandra* imaging, as a function of both $L_{1.4}^{\rm AGN}$ and redshift. However, our flux-limited radio sample is increasingly incomplete towards the faintest radio sources, at each redshift. If the X-ray properties of detected and undetected radio sources were intrinsically different, using an incomplete sample would likely bias our results. For this reason, we decided to further reduce our sample to a subsample of radio-excess AGNs that is complete in $L_{1.4}^{\rm AGN}$ up to a given redshift. Fig. 1 shows the 13 bins identified in the $L_{1.4}^{\rm AGN}$–z space (shaded areas). This approach allows us to explore the simultaneous dependence of the SMBH accretion rate on both $L_{1.4}^{\rm AGN}$ and redshift, which is crucial for understanding which parameter primarily drives the accretion power in radio AGNs. This cut reduces our previous radio AGN sample to 1272 sources, out of which 213 (around 17 per cent) are X-ray detected. Table 1 summarizes the number of sources contained in each of the 13 $L_{1.4}^{\rm AGN}$–z bins, both detected and undetected in the X-rays. Our redshift grid at $0.6 < z < 5.0$ is optimized to ensure a good sampling of the highest radio luminosity sources, which are relatively uncommon within the volume covered by our survey at $z < 0.6$. Above this redshift, we note that all X-ray detected sources

Table 1. The number of radio-excess AGNs within the 13 complete $L_{1.4}^{\rm AGN}$–z bins. The numbers in brackets indicate the subset of X-ray detected (d) and not detected (u) sources, respectively.

z-bin	$\log(L_{1.4}^{\rm AGN})$ (W Hz^{-1})	# (d,u)
$0.6 \leq z < 1.0$	22.9–23.5	232 (33, 199)
	23.5–24.0	104 (25, 79)
	24.0–24.5	67 (15, 52)
	24.5–27.0	30 (10, 20)
$1.0 \leq z < 1.4$	23.5–24.0	122 (20, 102)
	24.0–24.5	57 (6, 51)
	24.5–27.0	42 (11, 31)
$1.4 \leq z < 1.8$	23.5–24.0	140 (20, 120)
	24.0–24.5	98 (15, 83)
	24.5–27.0	46 (9, 37)
$1.8 \leq z < 3.0$	24.0–24.5	133 (16, 117)
	24.5–27.0	148 (30, 118)
$3.0 \leq z < 5.0$	24.5–27.0	53 (3, 50)

have $L_{\rm X} > 10^{42}$ erg s^{-1}, which implies they are likely to be X-ray AGNs.

Despite this cut, our sample remains to date one of the largest and deepest data sets of well-defined radio-excess AGNs with full X-ray coverage and redshift information available.

3 CALCULATION OF THE INTRINSIC AGN X-RAY LUMINOSITY

In this Section we describe the method used to derive average SMBH accretion rates in each $L_{1.4}^{\rm AGN}$–z bin. These were derived from the mean X-ray emission obtained from *Chandra* stacks, as detailed below.

3.1 X-ray stacking

We stacked *Chandra* images taken from the joint *Chandra*-COSMOS and COSMOS-Legacy map (Civano et al. 2016; Marchesi et al. 2016a), at the optical/near-infrared position of each input source, both in the soft ([0.5–2] keV), hard ([2–8] keV), and full ([0.5–8] keV) X-ray bands.

For this task, we used the publicly available X-ray stacking tool CSTACK.[2] This online software returns stacked count rates and fluxes, as well as reliable uncertainties estimated from a bootstrapping procedure. The stacking procedure was run for each $L_{1.4}^{\rm AGN}$–z bin, by combining the signal from X-ray detections and non-detections.

We followed the same method built in CSTACK for deriving fluxes and uncertainties from stacking. Briefly, for each $L_{1.4}^{\rm AGN}$–z bin, we generated 1000 new input source lists, each created by randomly selecting the same total number of objects of the original list, but allowing duplication of the same source. We stacked each re-sampled data set and obtained a distribution of 1000 mean (in linear scale) fluxes for each $L_{1.4}^{\rm AGN}$–z bin. We considered the median value of the corresponding distribution as our best estimate of the stacked X-ray flux ($F_{\rm X}$) associated with that bin. Flux uncertainties ($dF_{\rm X}$, at 1 σ level) were estimated by interpolating the above distribution at the 16th and 84thpercentiles. This approach enabled us to mitigate the effect of possible outliers in the underlying distribution of X-ray fluxes.

The median stacked flux derived in each $L_{1.4}^{\rm AGN}$–z bin was then converted to rest-frame X-ray luminosity ($L_{\rm X}$) in each X-ray band, by assuming a power-law X-ray spectrum with an observed slope $\Gamma = 1.4$, consistently with the shape of the cosmic X-ray background (e.g. Gilli, Comastri & Hasinger 2007). The stacking procedure yielded $F_{\rm X}/dF_{\rm X} > 2$ in all bins. We note that each stacked image displays a significant detection with signal-to-noise S/N > 5, where N was measured from the background region around the centre of each stacked image. However, throughout the paper we used $dF_{\rm X}$ as a conservative estimate of the uncertainty on the stacked flux.

[2]Developed by T. Miyaji, CSTACK is available at http://lambic.astrosen.unam.mx/cstack/.

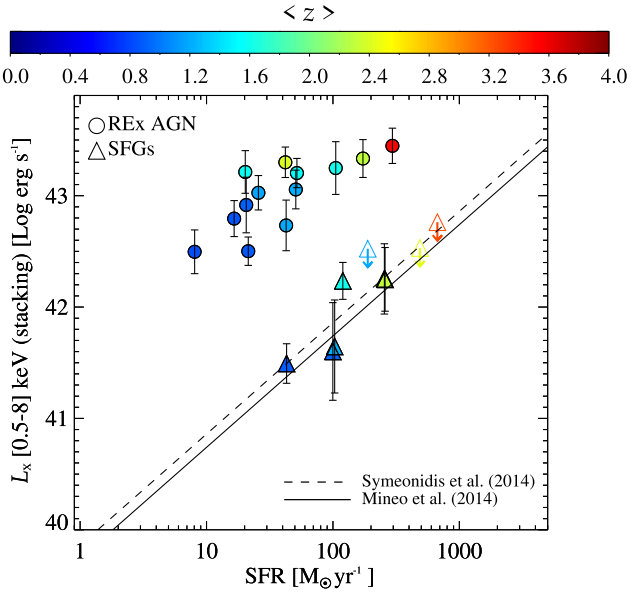

Figure 2. Comparison between the rest-frame [0.5–8] keV luminosity obtained from *Chandra* stacking (colour coded with redshift), and the (linear) mean SFR calculated from SED fitting. The dashed line indicates the $L_{\rm X}$–SFR relation of Symeonidis et al. (2014), while the dotted–dashed line marks a similar relation independently proposed by Mineo et al. (2014). Radio-excess AGNs are shown as circles, while the control sample of redshift-matched SFGs is marked with triangles. See the text for details.

3.2 Subtraction of X-ray emission due to star formation

We investigated the origin of the stacked X-ray emission derived in the previous Section. While X-ray emission in individually detected sources mostly arises from the AGN, for X-ray undetected sources the possible contribution of star formation might not be negligible.

We employed the empirical relation between SFR and X-ray luminosity presented in Symeonidis et al. (2014) to estimate and then subtract the X-ray emission expected to arise from star formation. This relation was calibrated on a sample of star-forming galaxies selected with *Herschel* at $z < 1.5$ in the *Chandra* Deep Field South (CDF-S), both detected and undetected in the X-rays. We estimated the SFR for each radio source from the corresponding total IR (8–1000 μm) luminosity obtained from an SED decomposition, after correcting for a possible AGN contribution (see D17).

Fig. 2 illustrates the comparison between the rest-frame [0.5–8] keV luminosity obtained from stacking (see Section 3.1) in the various redshift bins (in colour coding), and the (linear) mean SFR of

the underlying radio-excess AGN population (circles). The dashed line indicates the L_X–SFR relation of Symeonidis et al. (2014), which carries a 1 σ scatter of about a factor of 2, here scaled to the [0.5–8] keV energy range. The dotted–dashed line marks a similar relation independently proposed by Mineo et al. (2014), shown here for comparison.

The stacked L_X obtained in each bin displays a systematic and significant (1.2–2.2 dex) excess with respect to the X-ray emission expected from star formation, which suggests the presence of widespread AGN activity in each stacked bin. As a sanity check, we repeated the same stacking procedure for a redshift-matched control sample of (non-AGN) radio-detected star-forming galaxies (SFGs, see triangles in Fig. 2), which constitute the same sample as the one previously used to calculate the q_{SF} parameter. For those bins in which X-ray stacking yielded no detection, we placed upper limits at the 90th per cent confidence level (downward arrows) via bootstrapping (see Section 3.1). Fig. 2 shows a very good agreement at all redshifts between the mean X-ray luminosities of our SFGs and those expected on the basis of the Symeonidis et al. (2014) and Mineo et al. (2014) L_X–SFR relations. This check ensures the applicability of the L_X–SFR relation for our sample of radio-excess AGNs and throughout the full redshift range.

In each $L_{1.4}^{AGN}$–z bin, we used the Symeonidis et al. (2014) relation to estimate and then subtract the X-ray emission expected to arise from star formation, at the mean SFR of the stacked sample (<10 per cent in all bins). Only the AGN-related X-ray emission was considered in the next steps. The mean L_X values obtained from stacking are reported in Table 2, separately for the full radio-excess sample, and for the subset with X-ray detection. As shown in Table 2, the X-ray detected subsample displays, on average, 0.5–0.8 dex higher X-ray emission than that of the full (i.e. X-ray detected + undetected) radio-excess AGN sample. We stress that a weaker (0.3–1.5 dex), but systematic X-ray excess would be still in place if only undetected X-ray sources were considered. This implies that, also below the *Chandra* detection limit, a significant fraction of the stacked X-ray emission is arising from active SMBH accretion.

3.3 Correction for nuclear obscuration

The AGN-related X-ray emission derived from *Chandra* stacking might be underestimated due to nuclear obscuration. In this Section, we correct the stacked X-ray emission for this effect via the Hardness Ratio (HR), by following the procedure adopted by Marchesi et al. (2016a). The HR is defined as $HR = \frac{H-S}{H+S}$, where (H, S) represent the (exposure weighted) photon counts in the hard (2–8 keV) and soft (0.5–2 keV) bands, respectively.

A large fraction (about 85 per cent) of our input sources are individually undetected in all *Chandra* bands. In the low-count regime, uncertainties do not follow a Gaussian distribution and should be treated in a more appropriate way. The *Bayesian Estimation of Hardness Ratios* (BEHR) method (Park et al. 2006) is particularly effective for faint X-ray sources, because it does not need a detection in both bands to work and it runs a Bayesian Markov chain Monte Carlo calculation to estimate errors. Starting from the (H, S) values obtained from X-ray stacking in each bin, we ran BEHR recursively by comparing – at each iteration – the observed HR inferred with the BEHR to an intrinsic (i.e. unabsorbed) X-ray spectral model, which was assumed to be a power-law spectrum with a photon index $\Gamma = 1.8$ (e.g. Tozzi et al. 2006). This method allowed us to obtain a rough estimate of the average nuclear obscuration, which we used

Table 2. Main parameters (and corresponding 1 σ uncertainties) obtained via X-ray stacking in each $L_{1.4}^{AGN}$–z bin. We calculated the mean value of each parameter, separately for all radio-excess AGNs (both X-ray detected and undetected, see the tag 'all'), and for the X-ray detected subset alone (see the tag 'det'). The tag L_X corresponds to the [0.5–8] keV X-ray luminosity obtained from *Chandra* stacking, while the tag L_X^{AGN} represents the intrinsic AGN X-ray luminosity.

z-bin	$L_{1.4}^{AGN}$	L_X	L_X	HR	HR	L_X^{AGN}	L_X^{AGN}	s-BHAR	s-BHAR	$\log(\lambda_{edd})$	$\log(\lambda_{edd})$
	$\log(W\,Hz^{-1})$	$\log(erg\,s^{-1})$ (all)	$\log(erg\,s^{-1})$ (det)	(all)	(det)	$\log(erg\,s^{-1})$ (all)	$\log(erg\,s^{-1})$ (det)	$\log(erg\,s^{-1}\,M_\odot^{-1})$ (all)	$\log(erg\,s^{-1}\,M_\odot^{-1})$ (det)	(all)	(det)
$0.6 \leq z < 1.0$	22.9–23.5	42.50 ± 0.18	43.25 ± 0.18	-0.29 ± 0.40	-0.09 ± 0.12	42.61 ± 0.21	43.44 ± 0.20	32.35 ± 0.20	33.25 ± 0.23	-3.06 ± 0.20	-2.15 ± 0.23
	23.5–24.0	42.79 ± 0.15	43.41 ± 0.13	0.04 ± 0.28	0.09 ± 0.11	43.01 ± 0.17	43.64 ± 0.15	32.71 ± 0.18	33.35 ± 0.18	-2.69 ± 0.18	-2.05 ± 0.18
	24.0–24.5	42.50 ± 0.11	43.03 ± 0.11	0.05 ± 0.49	0.08 ± 0.17	42.71 ± 0.13	43.25 ± 0.12	32.35 ± 0.13	33.04 ± 0.13	-3.05 ± 0.13	-2.36 ± 0.13
	24.5–27.0	42.92 ± 0.23	43.46 ± 0.18	-0.15 ± 0.25	-0.15 ± 0.12	43.08 ± 0.27	43.63 ± 0.22	32.69 ± 0.29	33.30 ± 0.24	-2.71 ± 0.29	-2.10 ± 0.24
$1.0 \leq z < 1.4$	23.5–24.0	43.03 ± 0.14	43.65 ± 0.15	0.06 ± 0.30	0.05 ± 0.11	43.25 ± 0.17	43.87 ± 0.16	32.96 ± 0.19	33.62 ± 0.18	-2.44 ± 0.19	-1.79 ± 0.18
	24.0–24.5	42.73 ± 0.21	43.58 ± 0.16	-0.13 ± 0.47	-0.06 ± 0.12	42.89 ± 0.23	43.78 ± 0.18	32.55 ± 0.24	33.62 ± 0.22	-2.85 ± 0.24	-1.78 ± 0.22
	24.5–27.0	43.06 ± 0.15	43.61 ± 0.13	-0.10 ± 0.31	-0.05 ± 0.13	43.23 ± 0.17	43.81 ± 0.14	32.84 ± 0.19	33.51 ± 0.16	-2.56 ± 0.19	-1.89 ± 0.16
$1.4 \leq z < 1.8$	23.5–24.0	43.21 ± 0.18	43.97 ± 0.18	-0.12 ± 0.36	-0.12 ± 0.11	43.39 ± 0.20	44.15 ± 0.21	33.36 ± 0.23	34.15 ± 0.25	-2.04 ± 0.23	-1.25 ± 0.25
	24.0–24.5	43.20 ± 0.12	43.77 ± 0.09	-0.00 ± 0.36	0.01 ± 0.13	43.41 ± 0.14	43.99 ± 0.10	33.16 ± 0.15	33.90 ± 0.12	-2.24 ± 0.15	-1.50 ± 0.12
	24.5–27.0	43.25 ± 0.20	43.89 ± 0.20	-0.15 ± 0.37	-0.16 ± 0.12	43.40 ± 0.23	44.05 ± 0.22	33.12 ± 0.27	33.84 ± 0.27	-2.28 ± 0.27	-1.56 ± 0.27
$1.8 \leq z < 3.0$	24.0–24.5	43.30 ± 0.13	44.15 ± 0.11	0.02 ± 0.50	-0.03 ± 0.13	43.53 ± 0.15	44.37 ± 0.12	33.56 ± 0.17	34.42 ± 0.15	-1.84 ± 0.17	-0.98 ± 0.15
	24.5–27.0	43.33 ± 0.16	43.98 ± 0.14	0.04 ± 0.50	0.06 ± 0.17	43.55 ± 0.18	44.22 ± 0.16	33.32 ± 0.20	33.98 ± 0.20	-2.08 ± 0.20	-1.42 ± 0.20
$3.0 \leq z < 5.0$	24.5–27.0	43.45 ± 0.14	44.26 ± 0.07	0.14 ± 0.42	0.28 ± 0.13	43.68 ± 0.18	44.57 ± 0.09	33.67 ± 0.22	34.62 ± 0.11	-1.73 ± 0.22	-0.78 ± 0.11

to calculate the mean absorption-corrected AGN X-ray luminosity ($L_{\rm X}^{\rm AGN}$) and its uncertainty in each $L_{1.4}^{\rm AGN}$–z bin. The average obscuration correction factor to the [0.5–8] keV AGN X-ray luminosity ranges from 1.3 to 1.8, independently of $L_{1.4}^{\rm AGN}$ or redshift. The HR values calculated with the BEHR are listed in Table 2, separately for the full radio-excess AGN sample and the subset with X-ray detection. The HR values are consistent between these two populations within the 1 σ uncertainties.

We note that the level of obscuration based on the HR might be poorly constrained in the case of highly obscured AGNs (Xue et al. 2011), therefore we cross-matched our sample with the subset of 67 Compton Thick (i.e. with hydrogen column density $N_{\rm H} > 1.5 \times 10^{24}$ cm^{-2}) AGN candidates identified from X-ray spectral analysis in the *Chandra* Legacy survey (Lanzuisi et al. 2018; see also Marchesi et al. 2016b). We found only 11 common matches in total (11/67 $\sim$ 16 per cent, higher than, but consistent with the fraction of X-ray selected AGNs in COSMOS that are also radio-excess AGNs, 11 per cent), suggesting that the average intrinsic X-ray emission of radio-excess AGNs might not arise primarily from highly obscured AGN accretion. Our typical $N_{\rm H}$ estimates span the range $10^{22–23}$ cm^{-2}, suggesting a moderate level of obscuration. In this $N_{\rm H}$ regime, previous studies have shown that HR-based $N_{\rm H}$ estimates agree fairly well with those based on X-ray spectra (e.g. Xue et al. 2011).

4 RESULTS

We used the $L_{\rm X}^{\rm AGN}$ estimates derived in Section 3.3 to study the simultaneous dependence of $L_{\rm X}^{\rm AGN}$ on $L_{1.4}^{\rm AGN}$ and redshift.

4.1 Average $L_{\rm X}^{\rm AGN}$ of radio-excess AGNs

Fig. 3 (panel *a*) illustrates the average absorption-corrected $L_{\rm X}^{\rm AGN}$ as a function of $L_{1.4}^{\rm AGN}$–z and separately in each redshift bin. We calculated the 1 σ uncertainties on the derived $L_{\rm X}^{\rm AGN}$ (see Section 3.3) by propagating the uncertainties on both the subtraction of X-ray star formation and the correction for nuclear obscuration, via a Monte Carlo approach. These plots show a strong increase of $L_{\rm X}^{\rm AGN}$ with redshift, at fixed $L_{1.4}^{\rm AGN}$, while no clear trend appears as a function of $L_{1.4}^{\rm AGN}$, within the same redshift bin. These findings suggest that the AGN radiative power traced by X-ray emission is not tightly tied to the radio AGN power traced by our VLA data, in a statistical sense. In addition, and especially for the highest $L_{1.4}^{\rm AGN}$ range, our results highlight an enhancement of the average $L_{\rm X}^{\rm AGN}$ from $z \sim 0.7$ to 3.5 by a factor of about 4.

We remind the reader that our radio-excess AGN sample is complete in radio luminosity in each $L_{1.4}^{\rm AGN}$–z bin. This ensures that our observed trends are not affected by obvious selection effects. We also stress that the stronger redshift dependence seen here is not driven by X-ray emission being boosted by a few bright detections. As shown in Table 1, the fraction of X-ray detections increases for brighter radio sources and at lower redshifts. If our $L_{\rm X}^{\rm AGN}$ estimates were biased high due to bright X-ray outliers, we would expect to see $L_{\rm X}^{\rm AGN}$ to resemble the same trend of the fraction of X-ray detections. On the contrary, we observed a flat trend between $L_{\rm X}^{\rm AGN}$ and $L_{1.4}^{\rm AGN}$, and a positive evolution of $L_{\rm X}^{\rm AGN}$ with redshift (see panel *a* of Fig. 3). This check suggests that the relative fraction of X-ray detected or undetected sources within a given bin does not significantly affect the average X-ray emission obtained from stacking. The only mild enhancement of $L_{\rm X}^{\rm AGN}$ with $L_{1.4}^{\rm AGN}$ can be identified in the lowest redshift bin, though marginally consistent also with a flat trend. This apparent increase may be partly attributed to the relatively high fraction of X-ray detections in the highest $L_{1.4}^{\rm AGN}$ bin (33 per cent against an average 16 per cent), as shown in Table 1.

4.2 From $L_{\rm X}^{\rm AGN}$ to specific SMBH accretion rate

We used the X-ray luminosity obtained from stacking to derive the average SMBH accretion rate, in each $L_{1.4}^{\rm AGN}$–z bin. We converted the average absorption-corrected $L_{\rm X}^{\rm AGN}$ to SMBH accretion rate by using a set of scaling factors. Each intrinsic $L_{\rm X}^{\rm AGN}$ was first scaled to bolometric AGN luminosity ($L_{\rm bol}$) via a set of luminosity-dependent bolometric corrections (Lusso et al. 2012), and then turned into SMBH accretion rate, by assuming a constant matter-to-radiation conversion efficiency of 0.1 (see review by Alexander & Hickox 2012). Finally, this parameter was converted to $\lambda_{\rm edd}$ by assuming a constant ratio between SMBH mass ($M_{\rm BH}$) and $M_\star$ of 0.002 (e.g. Häring & Rix 2004). The latter assumption carries severe uncertainties, and it is poorly constrained for non-local AGNs, especially if not type-1, unobscured systems (e.g. Ricci et al. 2017). For this reason, we expressed the $\lambda_{\rm edd}$ in terms of 'specific SMBH accretion rate' (s-BHAR), which is defined as $L_{\rm bol}$ normalized to the $M_\star$ of the host (see Aird et al. 2012). This parameter is roughly equivalent to $\lambda_{\rm edd}$, though it does not assume a specific conversion from $M_{\rm BH}$ to $M_\star$.

Fig. 3 (panel *b*) shows the average s-BHAR (or $\lambda_{\rm edd}$) as a function of $L_{1.4}^{\rm AGN}$, in each redshift bin. An equivalent plot is shown in Fig. 4 with the average s-BHAR colour coded in the $L_{1.4}^{\rm AGN}$–z diagram. From these plots, the average s-BHAR appears to increase with redshift, at fixed $L_{1.4}^{\rm AGN}$, while the trend with $L_{1.4}^{\rm AGN}$ is consistent with being flat, within any given redshift bin. We note that the error bars displayed in Fig. 3 reflect the same sources of uncertainties discussed in 4.1, simply scaled to s-BHAR (or $\lambda_{\rm edd}$). Mean s-BHAR and $\lambda_{\rm edd}$ values are listed in Table 2 with their corresponding 1 σ uncertainties, for both the full radio-excess AGN sample and for the X-ray detected subsample alone.

The rising trend of s-BHAR with redshift appears stronger than that observed for the average $L_{\rm X}^{\rm AGN}$. This is partly due to the luminosity-dependent bolometric correction, but also to the SMBH accretion rate being normalized to the host galaxy $M_\star$. Indeed, the average galaxy $M_\star$ tends to decrease with increasing redshift, since galaxies at earlier cosmic epochs have not built up their full stellar content. These factors slightly amplify the previous redshift trend seen with $L_{\rm X}^{\rm AGN}$, leading to the average s-BHAR increase by a factor of $\sim$10 from $z \sim 0.7$ to 3.5, in the highest 1.4 GHz luminosity range ($10^{24.5} < L_{1.4}^{\rm AGN} < 10^{27}$ W Hz^{-1}). While the full redshift range ($0.6 < z < 5.0$, split in five bins) can be explored for the brightest radio sources, we note that a smaller redshift window is accessible for fainter radio sources, counting four (three) redshift bins for the 1.4 GHz luminosity range $10^{24} < L_{1.4}^{\rm AGN} < 10^{24.5}$ W Hz^{-1} ($10^{23.5} < L_{1.4}^{\rm AGN} < 10^{24}$ W Hz^{-1}). However, the redshift increase is observed in all $L_{1.4}^{\rm AGN}$ bins.

In particular, at $z > 2$ the average s-BHAR corresponds to $\lambda_{\rm edd} \gtrsim 1$ per cent, implying that the typical radio AGN activity can be approximately described with radiatively efficient accretion (e.g. Merloni & Heinz 2008). We acknowledge the notably high uncertainties and possible systematics of the derived $\lambda_{\rm edd}$ estimates, thus we caution the reader that different scaling factors might lead to a wide range of $\lambda_{\rm edd}$ values. None the less, under the basic assumption that the above-mentioned scaling factors apply regardless of $L_{1.4}^{\rm AGN}$ and redshift, our results suggest that radio AGNs with a given jet power (or $L_{1.4}^{\rm AGN}$) become more and more radiatively efficient from

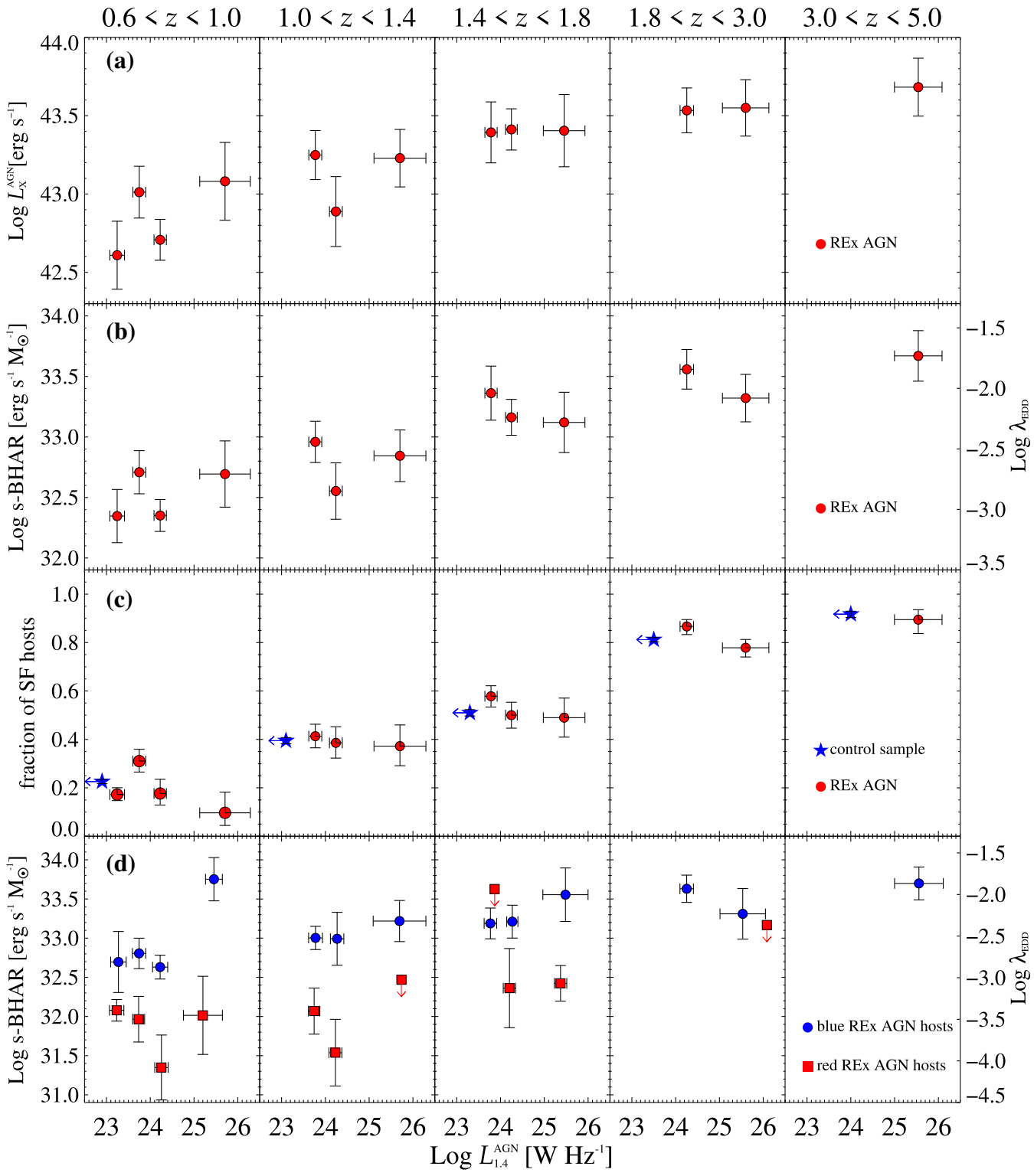

Figure 3. Average parameters (y-axis), as a function of $L_{1.4}^{AGN}$ (x-axis), separately in different redshift bins. In each panel, the horizontal error bars indicate the $1\,\sigma$ dispersion in $L_{1.4}^{AGN}$ of the underlying sample, while the vertical error bars indicate the corresponding σ uncertainty. The plot consists in four sets of panels. (a): Average L_X^{AGN} obtained from stacking (Section 4.1) after subtracting the star formation contribution (Section 3.2) and correcting for nuclear obscuration (Section 3.3). (b): Average s-BHAR (or λ_{edd}) obtained after scaling L_X^{AGN} to bolometric AGN luminosity, and assuming a matter-to-radiation conversion efficiency of 0.1 (Section 4.2). (c): Fraction of (blue) star-forming radio AGN hosts, based on the $(NUV - r)/(r - J)$ diagram (Section 4.3). The $\pm1\,\sigma$ uncertainties were derived by following Gehrels (1986). Red circles indicate radio-excess AGNs, while blue stars refer to a control sample of non-AGN galaxies matched in $M_\star$ and redshift. The left-pointing arrows indicate the 3 GHz luminosity ($5\,\sigma$) limit of our survey at the mean redshift of the underlying sample (scaled to 1.4 GHz by assuming a spectral index $\alpha = -0.7$). (d): Average s-BHAR (or λ_{edd}) derived separately for blue (circles) and red (squares) radio-excess AGN hosts, based on the $(NUV - r)/(r - J)$ diagram (Section 4.3 and Fig. 5). Down-pointing arrows indicate upper limits at 90 per cent confidence level.

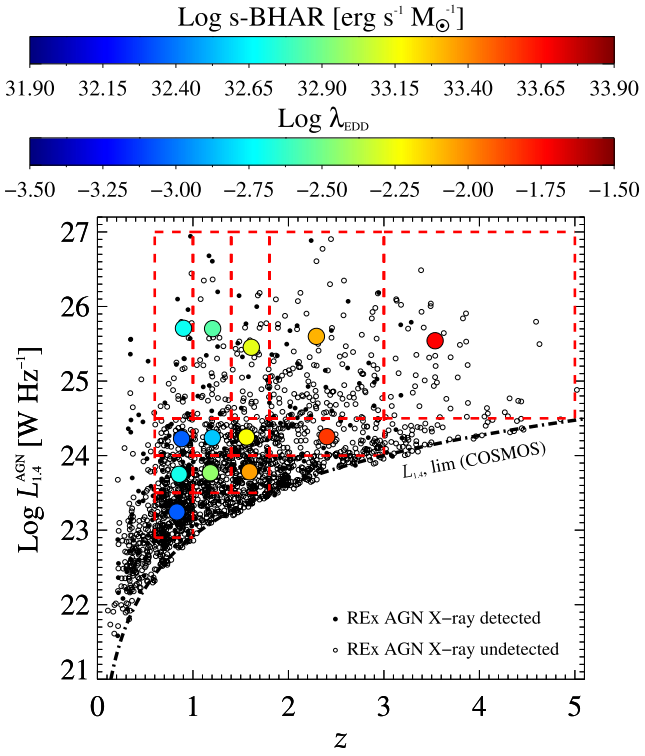

Figure 4. Average s-BHAR (or λ_{edd}, in colour coding) derived in each complete $L_{1.4}^{AGN}$–z bin via X-ray stacking of both detected and undetected X-ray sources.

low to high redshift. A more detailed discussion of the implications of these findings is given in Section 5.

4.3 Colours of radio-excess AGN hosts

In this Section we explore the star-forming properties of galaxies hosting radio-excess AGNs. The reason for this analysis is to investigate whether the trends of s-BHAR as a function of redshift and $L_{1.4}^{AGN}$ seen in Section 4.2 are linked to the integrated properties of the host galaxy. For each radio-excess AGN, we have an optical-NIR counterpart from the COSMOS2015 catalogue of Laigle et al. (2016). Each entry lists *K*-corrected absolute magnitudes in the rest-frame *NUV*, *r*, and *J* bands, which we used to plot our galaxies in the colour–colour diagram $(NUV - r)/(r - J)$. Then we used the following empirical expressions from Davidzon et al. (2017):

$$(NUV - r) = 3(r - J) + 1 \quad \text{and} \quad (NUV - r) > 3.1 \qquad (1)$$

to set the dividing line between quiescent galaxies (above the locus) and SFGs (below the locus), which roughly corresponds to a cut in specific SFR (s-SFR = SFR/$M_\star$; Ilbert et al. 2013). Our Fig. 5 shows the distribution of radio-excess AGNs analysed in this work (circles) over the $(NUV - r)/(r - J)$ diagram. The black solid line corresponds to equation (1): this line does not separately classify galaxies within the so-called 'green valley', i.e. the intermediate wedge between quiescent and star-forming systems. To account for this effect, we conservatively select as ('blue') SFGs only those sources lying more than 0.5 mag below equation (1) (i.e. blue circles in Fig. 5). This colour–colour diagram reduces the possible misclassification of highly dust-obscured galaxies as passive systems, and it has been proved to be effective also at $z > 4$ (see fig. 7 in Davidzon et al. 2017).

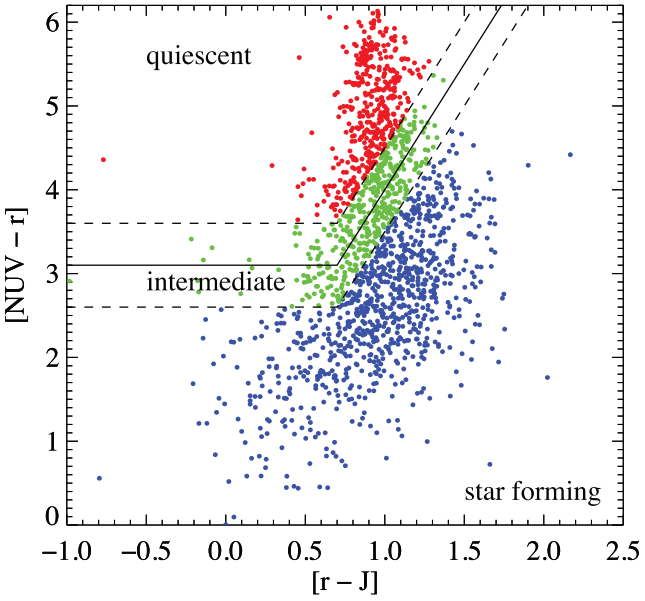

Figure 5. Rest-frame $(NUV - r)$ versus $(r - J)$ diagram. The dashed lines mark the intermediate wedge centred on the solid line (equation 1), which separates quiescent (upper-left corner) and star-forming galaxies (lower-right corner). Circles indicate the radio-excess AGN sample studied in this work, whose hosts are classified based on the $(NUV - r)/(r - J)$ as quiescent (red), intermediate (green), or star forming (blue). See the text for details.

Following this approach, we calculated the fraction of star-forming hosts (f_{SF}) within our radio-excess AGN sample, as a function of $L_{1.4}^{AGN}$ and redshift. Fig. 3 (panel *c*) shows the derived f_{SF} estimates for radio-excess AGNs (red circles), while the error bars indicate their corresponding $\pm 1\,\sigma$ confidence interval (according to equations 23–24 from Gehrels 1986). Fig. 3 suggests a strong increase of f_{SF} with redshift, at fixed $L_{1.4}^{AGN}$, at least up to $z \sim 2$, while there is no, or at most a weakly decreasing trend with $L_{1.4}^{AGN}$, at fixed redshift.

These observed trends are qualitatively similar to those seen for the s-BHAR (or λ_{edd}) in Section 4.2. This similarity might imply a link, in a statistical sense, between the average AGN radiative power and active star formation within radio-excess AGN hosts. A positive correlation between BHAR and SFR has been previously documented for IR-selected samples of galaxies (Chen et al. 2013; Delvecchio et al. 2015), and justified via numerical simulations under the assumption of a common fuelling mechanism for both SMBH accretion and galaxy star formation (e.g. McAlpine et al. 2017). However, hints of such a correlation have never been observed for radio AGN hosts, mostly because of the lack of deep and uniform radio data across a wide $L_{1.4}^{AGN}$ and redshift range.

As a sanity check, we investigated whether a similar trend could be observed for a control sample of 'inactive' galaxies (i.e. not radio-excess AGNs) matched in $M_\star$ and redshift. This latter sample was selected from the full COSMOS2015 catalogue (Laigle et al. 2016), after eliminating all radio-excess AGNs (from this work) and sources within masked areas in the optical/NIR images. This sample was then split in five redshift bins, as previously done for our radio-excess AGNs. Within each bin, we randomly selected a subset of COSMOS2015 sources in different $M_\star$ bins, in order to match the $M_\star$ distribution observed for radio-excess AGNs. We applied this method to all redshift bins, and retrieved the $(NUV - r)/(r - J)$ colours for each randomly selected source. The blue stars in Fig. 3 (panel *c*) mark the f_{SF} values for the above-mentioned

control sample. Since this mainly consists of VLA 3 GHz undetected sources (though not necessarily, since there might be a subset of radio-detected SFGs), we place an indicative upper limit to $L_{1.4}^{\rm AGN}$ (see the left-pointing arrow in panel *c* of Fig. 3), consistent with the $5\,\sigma$ luminosity limit of our 3 GHz survey. Each upper limit was centred at the mean redshift of the underlying population and scaled to 1.4 GHz by assuming a single power-law spectrum with a spectral index $\alpha = -0.7$ (e.g. Condon 1992).

The $f_{\rm SF}$ estimates derived for this control sample are in good agreement with those calculated for radio-excess AGNs within the same redshift bin. While it is well accepted that radio AGN activity is more prevalent in massive galaxies (Fabian 2012; Morganti et al. 2013), these findings (Fig. 3, panel *c*) suggest that, at fixed $M_\star$ and redshift, the triggering of radio AGN activity is independent of the colour and star-forming properties of the host galaxy. These results broadly support the idea that the overall fraction of star-forming galaxies significantly increases with redshift, regardless of $L_{1.4}^{\rm AGN}$, which might explain the similar redshift dependence seen for the average s-BHAR in radio AGNs.

5 DISCUSSION

We analysed a complete, well-defined sample of radio-excess AGNs selected at 3 GHz in the COSMOS field. Stacking of deep X-ray images obtained with *Chandra* was performed for 1272 radio AGNs across a wide luminosity and redshift range, which allowed us to infer the average $L_{\rm X}^{\rm AGN}$ and s-BHAR in each bin. In this Section, we discuss and interpret the observed trends of s-BHAR as a function of $L_{1.4}^{\rm AGN}$ and redshift. The average estimates of the AGN radiative power obtained from X-ray stacking (Section 4.2) display a positive evolution with redshift, yielding $\lambda_{\rm edd}$ values consistent with radiatively efficient SMBH accretion ($\lambda_{\rm edd} \gtrsim 1$ per cent) at $z \gtrsim 2$, at fixed 1.4 GHz luminosity $L_{1.4}^{\rm AGN}$. We also observed a qualitatively similar evolution in the fraction of star-forming host galaxies, possibly hinting at a connection between AGN radiative power and active star formation in radio AGN hosts. In order to investigate further what might be driving the observed trends, we discuss the main properties of radio-excess AGN hosts and compare our results with previous studies in the literature.

5.1 Radio-excess AGN hosts through cosmic time

The AGN radiative power traced by X-ray emission is commonly associated with ongoing SMBH accretion (e.g. Alexander & Hickox 2012). Several observational studies pointed out that the volume-averaged SMBH accretion density and SFR density evolve in a similar fashion, both peaking at redshift $z \sim 1$–3 (e.g. Madau & Dickinson 2014), which thereby suggests a statistical co-evolution between AGN and galaxy growth. It is widely accepted that SMBH growth and galaxy star formation are both fuelled via cold gas accretion. Indeed, X-ray AGNs, tracing the radiative phase of SMBH accretion, have been found to prefer star-forming, gas-rich galaxies (Rosario et al. 2013; Vito et al. 2014). Moreover, the intrinsic s-BHAR distribution of AGNs was found to shift towards higher values with increasing redshift, at fixed $M_\star$, and especially in star-forming galaxies (e.g. Aird et al. 2018). These findings support the idea of cold gas being the key ingredient for triggering AGN and star formation activity.

In Section 4.3, we examined the star-forming content of radio-excess AGN hosts by exploiting the $(NUV - r)/(r - J)$ colours as dust-insensitive tracers of active star formation. Previous studies investigating the properties of radio AGN hosts have relied on the presence of *Herschel* detection in the FIR to assess the star-forming content of the host (e.g. Magliocchetti et al. 2018). However, such a selection is limited by the *Herschel* sensitivity, which might be missing a substantial fraction of galaxies with relatively low SFRs, especially at high redshift. On the contrary, the $(NUV - r)/(r - J)$ selection used in this work has been proven to be effective in selecting typical main-sequence galaxies also at $z \gtrsim 4$ (e.g. Ilbert et al. 2013; Davidzon et al. 2017), in the absence of strong AGN contamination.

Fig. 3 (panel *c*) displays a weak trend of $f_{\rm SF}$ with $L_{1.4}^{\rm AGN}$, at fixed redshift, while the dependence on redshift appears significantly stronger. However, this redshift trend could be mainly driven by the cosmic evolution of the full galaxy population (see Section 4.3). Indeed, as mentioned in Section 4.3, we observed a similar $f_{\rm SF}$ behaviour for a control sample of (redshift and $M_\star$-matched) galaxies without radio excess. This implies that the overall galaxy population follows a similar transformation through cosmic time, regardless of whether an AGN is driving strong radio jets or not. According to this scenario, the cosmic evolution of galaxies is mainly driven by the evolution of their cold gas content, which may occasionally trigger and sustain AGN activity.

In fact, independent works found that star-forming galaxies around the 'main-sequence' relation (Noeske et al. 2007; Elbaz et al. 2011) become increasingly richer in cold gas ($M_{\rm gas}$) towards higher redshifts, with their molecular gas fraction ($f_{\rm gas} = M_{\rm gas}/M_\star$) steeply rising from $z \sim 0$ to 2–3 (Daddi et al. 2010; Tacconi et al. 2010; Geach et al. 2011; Magdis et al. 2012; Saintonge et al. 2012). Moreover, Gobat et al. (2017) found a surprisingly large dust and gas content in quiescent galaxies at $z \sim 1.8$, containing 2–3 orders of magnitude more dust, at fixed $M_\star$, than local quiescent galaxies. This indicates that early-type galaxies at $z > 1$ are not truly passive, but instead contain substantial amounts of cold gas (5–10 per cent), which could possibly sustain (though in a smaller contribution compared to SFGs) radiatively efficient SMBH accretion.

All these studies further corroborate the idea that (i) the high-redshift Universe facilitates radiative AGN activity and (ii) the evolution of the cold gas content shapes the cosmic transformation of galaxies.

In support of this interpretation, Fig. 3 (panel *d*) shows that the average s-BHAR calculated for radio-excess AGNs within 'blue' (circles) star-forming hosts is systematically ($>3\times$) higher than that derived for the 'red' (squares) quiescent subsample, based on the $(NUV - r)/(r - J)$ criterion. This difference is seen out to $z \sim 1.5$, while at $z \gtrsim 2$ the red subsample is either absent or shows upper limits (down-pointing arrows) due to poor statistics.

A simplistic cartoon shown in Fig. 6 summarizes this possible evolutionary scenario for radio AGNs. Broadly, a radio AGN with a given $L_{1.4}^{\rm AGN}$ undergoes a strong evolution of the average radiative AGN power from low to high redshift, reaching $\lambda_{\rm edd} \gtrsim 1$ per cent at $z \gtrsim 1.5$, independently of $L_{1.4}^{\rm AGN}$. In parallel, the overall galaxy population evolves with redshift from red and quiescent to blue and star-forming systems, regardless of whether a galaxy is hosting a radio AGN or not.

These results argue in favour of a connection between AGN radiative power and star-forming content of radio AGN hosts. Testing this picture for the overall galaxy population would require an $M_\star$-selected galaxy sample, as well as stacking deep X-ray/radio images to assess the radiative and kinetic AGN emission in galaxies at different cosmic epochs. Future work from our team will undertake such an analysis.

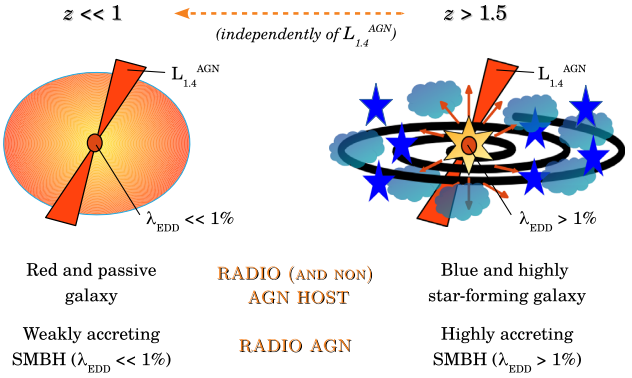

Figure 6. A simplistic cartoon summarizing a possible evolutionary scheme for radio-excess AGNs of a given radio power, based on the results of this work.

5.2 SMBH growth in radio-excess AGNs

Several studies argued that radio-excess AGNs are likely a mixture of radiatively efficient ('radiative mode') and inefficient ('jet mode') SMBHs, which have been found to evolve differently with cosmic time (Willott et al. 2001; Best et al. 2014; Pracy et al. 2016; Smolčić et al. 2017c; Novak et al. 2018). In particular, while radiative-mode AGNs roughly follow the evolution of the cosmic SFR density, consistently with them being fuelled via cold gas accretion, jet-mode AGNs display a decrease in space density that resembles the decline of massive quiescent galaxies with redshift (Best et al. 2014).

The strong redshift dependence seen in the average s-BHAR, at fixed $L_{1.4}^{\rm AGN}$ (panel *b* of Figs 3 and 4), is probably linked to the stronger cosmic evolution seen for the radiative-mode AGN population. An AGN synthesis model describing the various states in which SMBH growth may occur was presented by Merloni & Heinz (2008). This model postulates three accretion modes, as a function of $\lambda_{\rm edd}$ and released power: (i) the 'low-kinetic' mode, in which most of the power is released in a kinetic form, occurs below $\lambda_{\rm edd} \sim$ few per cent; (ii) the 'high radiative' mode, in which the power is mainly released in a radiative form with $\lambda_{\rm edd} >$ few per cent; (iii) the 'high-kinetic' mode, in which radiative and kinetic powers are both high ($\lambda_{\rm edd} >$ few per cent) and comparable. According to this model, in the radiatively efficient regime, radio-selected AGNs can trace both kinetic and radiative powers.

In the light of these considerations, the lack of correlation between s-BHAR and $L_{1.4}^{\rm AGN}$ seen in Fig. 3 (panel *b*), at fixed redshift, might be explained if synchrotron (radio) and accretion disc (X-ray) emission were statistically decoupled from one another, in a statistical sense. In addition, especially for the brightest radio sources, the different spatial scales at which AGN-driven X-ray (sub-pc) and radio (>kpc) emission processes operate could wash out possible hints of correlation.

On the other hand, the positive redshift dependence observed for a given $L_{1.4}^{\rm AGN}$ suggests that radio AGNs become more radiatively efficient towards early cosmic epochs. If the cosmic evolution of galaxies' colours is driven by their $f_{\rm gas}$, this trend also justifies the systematic increase in the average s-BHAR with redshift, thus reaching SMBH accretion rates consistent with the so-called high kinetic and high radiative modes ($\lambda_{\rm edd} >$ few per cent). Interestingly, our VLA-COSMOS data reveal that the average 3 GHz sizes of radio-excess AGNs at $z \sim 2$ appear to be significantly ($>3\,\sigma$) larger than those of their lower redshift ($z < 1$) analogues, at fixed radio luminosity (Bondi et al., in prep.). Since radiatively inefficient jet-mode accretion is usually associated with a compact radio core, an increasing size evolution might be the signature of a possible change in the typical accretion mode of radio AGNs. This idea is supported by observational studies finding that the intrinsic s-BHAR (or $\lambda_{\rm edd}$) distribution traced by X-ray emission shifts towards higher values with increasing redshift (Aird et al. 2018), and especially in star-forming systems. Understanding whether the average radio AGN emission follows the same trend would require an in-depth analysis of the overall $L_{\rm X}^{\rm AGN}/L_{1.4}^{\rm AGN}$ distribution, which will be presented in a separate paper (Delvecchio et al., in prep.).

We note that our sample of radio-excess AGNs achieves an unprecedented combination of completeness and sensitivity, and it does not exclusively consist of 'radio loud' AGNs (e.g. selected above a certain 1.4 GHz power). On the contrary, this sample spans the full 3 GHz flux density range down to $F_{\rm 3GHz} \sim 11$ μJy (i.e. $5\,\sigma$ sensitivity), which allows us to draw conclusions that are valid for the overall radio AGN population over a wide luminosity and redshift range. However, we acknowledge that a fraction of radio AGNs within the $L_{1.4}^{\rm AGN}$–z space analysed in this work might be missed, if this AGN-driven radio emission is washed out by the star formation contribution in radio, thus failing to meet the required $2\,\sigma$ cut in radio excess. We tested this possible incompleteness by relaxing the radio-excess threshold presented in Section 2.2 from $2\,\sigma$ to $1\,\sigma$. This increases the radio-excess sample (within the same $L_{1.4}^{\rm AGN}$–z space analysed in this work) by 40 per cent, especially towards faint 1.4 GHz luminosities. Though this change introduces more star-forming hosts within our sample, we verified that the main trends with redshift and $L_{1.4}^{\rm AGN}$ persist, thus confirming our previous results. However, we estimate that 1/3 of the newly selected (at $>1\,\sigma$ radio excess) AGNs might be contaminated by SFGs, which motivates our original choice of considering the $2\,\sigma$ radio-excess AGN sample. A more complete and unbiased view of radio AGN activity could be reached by combining deep VLA and high-resolution VLBI data (<0.01 arcsec) to overcome the problem of galaxy dilution towards fainter radio fluxes (e.g. Herrera Ruiz et al. 2017).

This work provides a comprehensive view of the cosmic behaviour of radio AGNs and their hosts. While previous studies, limited to radio-bright AGNs ($L_{1.4}^{\rm AGN} \gtrsim 10^{25}$ W Hz^{-1}) or intermediate redshifts ($z \lesssim 1$), found radio AGNs to reside within red and passive galaxies, our sample explores *both* fainter sources and higher redshifts. This allowed us to unveil a heterogeneous population of radio AGN hosts, displaying a strong cosmic evolution in terms of optical colours, star formation, and SMBH accretion rates. Though the mechanisms responsible for triggering radio AGN activity are still unconstrained, we argue that the presence of radio AGNs does not seem to affect the star-forming content of galaxies, at any redshift and radio luminosity. On the other hand, our results imply that radio AGNs, independently of their power, display a positive evolution in the AGN radiative power, gradually reaching a radiatively efficient accretion mode at $z \gtrsim 2$.

6 CONCLUSIONS

This work presents a comprehensive analysis of the average SMBH accretion properties of radio-excess AGNs. Our sample was originally selected from the VLA-COSMOS 3 GHz Large Project (Smolčić et al. 2017a), the deepest radio survey ever carried out in the COSMOS field. Our sample includes about 1800 radio-selected AGNs, which were identified via a ($>2\,\sigma$) radio excess relative to the IRRC of star-forming galaxies in the COSMOS field (Delhaize et al. 2017). To mitigate possible selection effects, we further

selected a subset of 1272 radio AGNs that is complete in $L_{1.4}^{\rm AGN}$, spanning the redshift range $0.6 < z < 5$ down to $L_{1.4}^{\rm AGN} \sim 10^{23}$ W Hz^{-1}. This sample allowed us to explore the average SMBH accretion properties *simultaneously* as a function of $L_{1.4}^{\rm AGN}$ and redshift. We stacked deep and uniform *Chandra* images in 13 different bins of the $L_{1.4}^{\rm AGN}$–z space, in order to infer the average X-ray emission and SMBH accretion properties of radio-excess AGNs. We summarize our main conclusions as follows:

(i) The average $L_{\rm X}^{\rm AGN}$ of radio-excess AGNs displays a positive evolution with redshift, at all $L_{1.4}^{\rm AGN}$, while we observe no correlation with $L_{1.4}^{\rm AGN}$, at fixed redshift (see panel *a* of Fig. 3).

(ii) The average s-BHAR, tracing the AGN radiative power, increases by a factor of 10 from $z \sim 0.6$ to 3.5, at fixed $L_{1.4}^{\rm AGN}$ (see panel *b* of Figs 3 and 4). If expressed in terms of Eddington ratio, our results suggest that SMBH accretion in radio AGNs becomes radiatively efficient ($\lambda_{\rm edd} \gtrsim 1$ per cent) at $z \gtrsim 2$, differently from what is seen at lower redshift ($z \lesssim 1$) for radio-bright ($L_{1.4}^{\rm AGN} \gtrsim 10^{25}$ W Hz^{-1}) AGNs (e.g. Hickox et al. 2009).

(iii) The host galaxies of radio AGNs display a strong evolution in their $(NUV - r)/(r - J)$ colours, becoming progressively bluer and more star forming with redshift. The fraction of 'blue' radio AGN hosts (from the criterion of Davidzon et al. 2017) increases from 20 to >80 per cent across the redshift range $0.7 < z < 3.5$, roughly independently of the radio power (see panel *c* of Fig. 3). This redshift trend qualitatively resembles that observed for the average s-BHAR (or $\lambda_{\rm edd}$), possibly suggesting a statistical connection between star-forming content and radiative AGN activity (e.g. Vito et al. 2014). These two trends are consistent with a scenario in which the molecular gas content within the host galaxy drives both SMBH accretion and star formation in radio AGN hosts.

(iv) The strong evolution in the colours of radio AGN hosts is fully consistent with the average colours derived for a control sample of non-AGN galaxies, matched in redshift and $M_\star$ (see panel *c* of Fig. 3). This finding suggests that 'jet-mode' feedback traced by radio AGN activity does not significantly affect the overall evolution of galaxies' colours. Whatever the mechanisms responsible for triggering radio AGN activity are, they seem to work independently of the star-forming content of the host.

Our results challenge the (often assumed) association between radio AGN activity and red passive host, and we interpret our findings within a 'big picture' of AGN-galaxy evolution. This work shows that the overall population of galaxies follows a strong redshift evolution in terms of colours and star-forming content, at least out to $z \sim 2$. In this scenario, galaxies hosting radio AGNs are no exception, as they display a consistent behaviour with a control sample of ($M_\star$-matched) non-AGN galaxies, at all redshifts. Our data suggest that jet-driven AGN activity does not primarily influence the cosmic transformation of galaxies. On the other hand, the increasing availability of cold gas supply [indicated by the $(NUV - r)/(r - J)$ colours] in the high-redshift Universe appears to facilitate radiative AGN activity. This corroborates the idea that radio-emitting AGNs at high redshift ($z > 1.5$) do not exclusively trace jet-mode feedback, but rather a combination of both radiative and kinetic output, in which both accretion modes are effective and comparable. These clues might be useful for advancing our current understanding on how AGN feedback comes into play and how it regulates the evolution of galaxies at different cosmic epochs.

ACKNOWLEDGEMENTS

The authors are grateful to the anonymous referee for his/her constructive comments that improved the content of this manuscript. ID is grateful to Fabio La Franca and Giorgio Lanzuisi for useful discussions. ID, VS, MN, and JD acknowledge the European Union's Seventh Framework programme under grant agreement 337595 (ERC Starting Grant, 'CoSMass'). TM and CSTACK are supported by UNAM_DGAPA PAPIIT IN104216 and CONACyT 252531. DR and DMA acknowledge the support of the Science and Technology Facilities Council (STFC) through grant ST/P000541/1.

REFERENCES

Aird J. et al., 2012, ApJ, 746, 90
Aird J., Coil A. L., Georgakakis A., 2018, MNRAS, 474, 1225
Alexander D. M., Hickox R. C., 2012, New Astron. Rev., 56, 93
Arnouts S., Cristiani S., Moscardini L., Matarrese S., Lucchin F., Fontana A., Giallongo E., 1999, MNRAS, 310, 540
Baloković M., Smolčić V., Ivezić Ž., Zamorani G., Schinnerer E., Kelly B. C., 2012, ApJ, 759, 30
Benson A. J., Bower R. G., Frenk C. S., Lacey C. G., Baugh C. M., Cole S., 2003, ApJ, 599, 38
Berta S. et al., 2013, A&A, 551, A100
Best P. N., Heckman T. M., 2012, MNRAS, 421, 1569
Best P. N., Ker L. M., Simpson C., Rigby E. E., Sabater J., 2014, MNRAS, 445, 955
Bonzini M., Padovani P., Mainieri V., Kellermann K. I., Miller N., Rosati P., Tozzi P., Vattakunnel S., 2013, MNRAS, 436, 3759
Bonzini M. et al., 2015, MNRAS, 453, 1079
Bower R. G., Benson A. J., Malbon R., Helly J. C., Frenk C. S., Baugh C. M., Cole S., Lacey C. G., 2006, MNRAS, 370, 645
Bruzual G., Charlot S., 2003, MNRAS, 344, 1000
Calistro Rivera G. et al., 2017, MNRAS, 469, 3468
Cavagnolo K. W., McNamara B. R., Nulsen P. E. J., Carilli C. L., Jones C., Bîrzan L., 2010, ApJ, 720, 1066
Chabrier G., 2003, PASP, 115, 763
Chen C.-T. J. et al., 2013, ApJ, 773, 3
Cirasuolo M., Magliocchetti M., Celotti A., Danese L., 2003, MNRAS, 341, 993
Civano F. et al., 2016, ApJ, 819, 62
Condon J. J., 1992, ARA&A, 30, 575
Croton D. J. et al., 2016, ApJS, 222, 22
da Cunha E., Charlot S., Elbaz D., 2008, MNRAS, 388, 1595
Daddi E. et al., 2010, ApJ, 713, 686
Davidzon I. et al., 2017, A&A, 605, A70
Del Moro A. et al., 2013, A&A, 549, A59
Delhaize J. et al., 2017, A&A, 602, A4
Delvecchio I. et al., 2015, MNRAS, 449, 373
Delvecchio I. et al., 2017, A&A, 602, A3 (D17)
Elbaz D. et al., 2011, A&A, 533, A119
Fabian A. C., 2012, ARA&A, 50, 455
Fanidakis N. et al., 2012, MNRAS, 419, 2797
Feltre A., Hatziminaoglou E., Fritz J., Franceschini A., 2012, MNRAS, 426, 120
Fritz J., Franceschini A., Hatziminaoglou E., 2006, MNRAS, 366, 767
Geach J. E., Smail I., Moran S. M., MacArthur L. A., Lagos C. d. P., Edge A. C., 2011, ApJ, 730, L19
Gehrels N., 1986, ApJ, 303, 336
Gilli R., Comastri A., Hasinger G., 2007, A&A, 463, 79
Gobat R. et al., 2017, A&A, 599, A95
Goulding A. D. et al., 2014, ApJ, 783, 40
Griffin M. J. et al., 2010, A&A, 518, L3
Hardcastle M. J., Evans D. A., Croston J. H., 2007, MNRAS, 376, 1849
Häring N., Rix H.-W., 2004, ApJ, 604, L89
Heckman T. M., Best P. N., 2014, ARA&A, 52, 589
Herrera Ruiz N. et al., 2017, A&A, 607, A132

Hickox R. C., Alexander D. M., 2018, preprint (arXiv:1806.04680)
Hickox R. C. et al., 2009, ApJ, 696, 891
Hopkins P. F., Hernquist L., Cox T. J., Kereš D., 2008, ApJS, 175, 356
Ilbert O. et al., 2006, A&A, 457, 841
Ilbert O. et al., 2013, A&A, 556, A55
Ivison R. J. et al., 2010, A&A, 518, L31
Kellermann K. I., Sramek R., Schmidt M., Shaffer D. B., Green R., 1989, AJ, 98, 1195
Laigle C. et al., 2016, ApJS, 224, 24
Lanzuisi G. et al., 2018, MNRAS, 480, 2578
Lusso E. et al., 2012, MNRAS, 425, 623
Lutz D. et al., 2011, A&A, 532, A90
Madau P., Dickinson M., 2014, ARA&A, 52, 415
Magdis G. E. et al., 2012, ApJ, 758, L9
Magliocchetti M., Popesso P., Brusa M., Salvato M., 2018, MNRAS, 473, 2493
Magnelli B. et al., 2015, A&A, 573, A45
Mancuso C. et al., 2017, ApJ, 842, 95
Marchesi S. et al., 2016a, ApJ, 817, 34
Marchesi S. et al., 2016b, ApJ, 830, 100
McAlpine S., Bower R. G., Harrison C. M., Crain R. A., Schaller M., Schaye J., Theuns T., 2017, MNRAS, 468, 3395
Mendez A. J. et al., 2013, ApJ, 770, 40
Merloni A., Heinz S., 2008, MNRAS, 388, 1011
Miller N. A. et al., 2013, ApJS, 205, 13
Mineo S., Gilfanov M., Lehmer B. D., Morrison G. E., Sunyaev R., 2014, MNRAS, 437, 1698
Molnár D. C. et al., 2018, MNRAS, 475, 827
Morganti R., Fogasy J., Paragi Z., Oosterloo T., Orienti M., 2013, Science, 341, 1082
Murphy E. J., 2009, ApJ, 706, 482
Narayan R., Yi I., 1994, ApJ, 428, L13
Noeske K. G. et al., 2007, ApJ, 660, L43
Novak M., Smolcic V., Schinnerer E., Zamorani G., Delvecchio I., Bondi M., Delhaize J., 2018, A&A, 614, A47
Oke J. B., 1974, ApJS, 27, 21
Oliver S. J. et al., 2012, MNRAS, 424, 1614
Padovani P., 2016, A&AR, 24, 13
Padovani P., Bonzini M., Kellermann K. I., Miller N., Mainieri V., Tozzi P., 2015, MNRAS, 452, 1263
Park T., Kashyap V. L., Siemiginowska A., van Dyk D. A., Zezas A., Heinke C., Wargelin B. J., 2006, ApJ, 652, 610
Pilbratt G. L. et al., 2010, A&A, 518, L1
Poglitsch A. et al., 2010, A&A, 518, L2
Pracy M. B. et al., 2016, MNRAS, 460, 2
Ricci F. et al., 2017, MNRAS, 471, L41
Rosario D. J. et al., 2013, ApJ, 771, 63
Saintonge A. et al., 2012, ApJ, 758, 73
Salvato M. et al., 2009, ApJ, 690, 1250
Salvato M. et al., 2011, ApJ, 742, 61
Sanders D. B., Soifer B. T., Elias J. H., Madore B. F., Matthews K., Neugebauer G., Scoville N. Z., 1988, ApJ, 325, 74
Sargent M. T. et al., 2010, ApJ, 714, L190
Schinnerer E. et al., 2010, ApJS, 188, 384
Scoville N. et al., 2007, ApJS, 172, 1
Shakura N. I., Sunyaev R. A., 1973, A&A, 24, 337
Smolčić V. et al., 2009, ApJ, 696, 24
Smolčić V. et al., 2017a, A&A, 602, A1
Smolčić V. et al., 2017b, A&A, 602, A2
Smolčić V. et al., 2017c, A&A, 602, A6
Spergel D. N. et al., 2003, ApJS, 148, 175
Symeonidis M. et al., 2014, MNRAS, 443, 3728
Tacconi L. J. et al., 2010, Nature, 463, 781
Tozzi P. et al., 2006, A&A, 451, 457
Vito F., Gilli R., Vignali C., Comastri A., Brusa M., Cappelluti N., Iwasawa K., 2014, MNRAS, 445, 3557
Willott C. J., Rawlings S., Blundell K. M., Lacy M., 1999, MNRAS, 309, 1017
Willott C. J., Rawlings S., Blundell K. M., Lacy M., Eales S. A., 2001, MNRAS, 322, 536
Xue Y. Q. et al., 2011, ApJS, 195, 10

This paper has been typeset from a TEX/LATEX file prepared by the author.